Physical and Numerical Modeling of Exposed Slag Eye in Continuous Casting Mold using Euler–Euler Approach

Zhongqiu Liu, Baokuan Li, Alexander Vakhrushev, Menghuai Wu, and Andreas Ludwig*

Gas injection through the submerged entry nozzle (SEN) into the continuous casting mold can be an effective approach for preventing SEN clogging and promoting the floatation of the non-metallic inclusions. However, sometimes the exposed slag eyes due to gas injection appear on the top surface of the liquid slag layer, resulting in heat losses, re-oxidation, and nitrogen pickup in the molten steel. An Eulerian multiphase-flow model is developed to predict the argon-steel-slag three-phase flow in a slab continuous casting mold. All the phases are treated based on Eulerian approach. The mathematical model is compared with the industrial observations and the water model experiments. Both of physical and numerical results reproduce the phenomenon of the high gas concentration at the SEN exit port. Most of the argon bubbles stay below the slag layer for quite long time because the slag blocks their floatation. Furthermore, the argon bubbles would gradually gather in a dense plume while escaping through the slag layer. Scattered argon exit spots are found at the top surface of slag layer. Two main locations of the exposed slag eye are found: 1) adjacent to the SEN; 2) at the mold's mid-section at the position where a concentrated argon plume breaches through the slag layer. The near-SEN exposed eye occurs under any of considered conditions. The one at the mid-section is formed when the meniscus convex reaches a critical level, been dependent on the casting conditions.

1. Introduction

Some industry operation measures during steel continuous casting, such as the argon gas injection, mold powder emulsification, non-metallic inclusion removal, and homogenization of molten steel, etc. induce very complex multiphase flow. In this sense, understanding the multiphase flow becomes ultimate important for controlling following problems of the production process[1–7]: a disturbed mold powder coverage or meniscus stagnation due to level fluctuations, the mold powder entrainment due to meniscus vortex and high surface velocity, the entrapment of the argon bubbles, and non-metallic inclusions by the solidified shell, and the thickness inhomogeneity and breakouts of initial solidification shell due to jet impingement, which have far-reaching consequences on the final product quality.

A mold flux is added periodically to the top surface of the continuous casting mold. It sinters and melts to form a protective liquid slag layer, which helps to prevent the oxidation of molten steel and absorb the non-metallic inclusions. In the meantime, argon gas injection is also introduced to prevent submerged entry nozzle (SEN) clogging, enhance the homogenization, and promote the floatation of the non-metallic inclusions. Due to the intense turbulent shear force inside the SEN, argon gas break-up into bubbles of various size distributions after exiting the SEN ports. The steel flow pattern inside the mold pool and the level fluctuations can altered by these argon bubbles.[8–10] However, that easily leads to increase of meniscus fluctuations, slag entrainment, and causes the liquid slag thinning, even initiating a formation of the exposed slag eye, which will result in heat losses, re-oxidation, and nitrogen pickup in the molten steel. **Figure 1** shows the formation of exposed slag eye in a twin slab caster mold, where the casting speed is $0.6\,\mathrm{m\,min^{-1}}$, argon injection rate is $5\,\mathrm{l\,min^{-1}}$ under the room temperature. Two kinds of slag open eyes can be defined, which are located symmetrically regarding the nozzle position: a smaller opening adjacent to the SEN and second (bigger one) located at about 0.4 m away from the SEN.

The formation of exposed slag eyes in the gas-stirred metallurgical vessels such as ladle[11–23] or tundish[24–26] is a common phenomenon. Extensive studies of the formation of exposed slag eyes in the ladle have been performed by physical[11–18] and numerical modeling.[19–23] For physical modeling, the water model experiments have been widely

Dr. Z. Liu, Prof. B. Li
School of Metallurgy
Northeastern University
No. 3-11, Wenhua Road, Heping District,
Shenyang 110819, P. R. China
E-mail: liuzq@smm.neu.edu.cn

Dr. Z. Liu, Dr. A. Vakhrushev, Prof. M. Wu
Christian Doppler Laboratory for Advanced Process Simulation of Solidification and Melting
University of Leoben
Austria

Prof. A. Ludwig
Chair of Simulation and Modeling of Metallurgical Processes
Department of Metallurgy
University of Leoben
Austria

DOI: 10.1002/srin.201800117

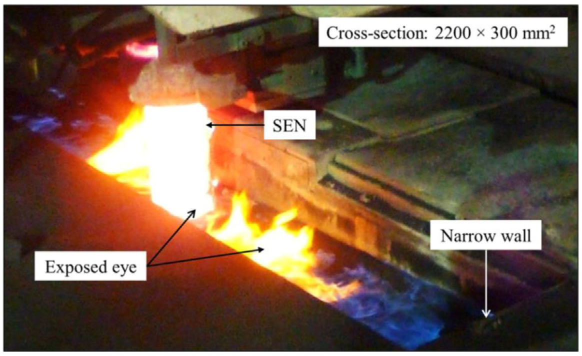

Figure 1. Industrial observation of the exposed slag eye.

used to study the sizes of slag eyes, various dimensionless expressions for exposed slag eye areas have been proposed by Yonezawa and Schwerdtfeger,[11,12] Subagyo et al.,[13] Iguchi et al.,[14] Mazumdar and Evans,[15] Krishnapisharody and Irons,[16,17] Liu et al.,[18] and so on. For numerical modeling, Li et al.,[19] Llanos et al.[20] developed a mathematical model based on volume of fluid (VOF) approach to analyse the argon/steel/slag three-phase flow and the exposed slag eye phenomenon in the ladle. Cloete et al.[21] and Liu et al.[22] developed a mathematical model by employing the discrete phase model (DPM) to describe the bubble transport and the VOF model to track the fluctuation of steel/slag interface without considering the bubble coalescence and breakup. Further Li et al.[23] developed a similar mathematical model by employing the DPM-VOF coupled method to investigate the slag layer and eye formation considering the bubble coalescence and breakup. Recently, the exposed slag eye formation in an inert gas-shrouded tundish has been studied by Chattopadhyay et al.,[24–26] a large number of experiments were done in a full scale and in a down-scaled water model under various operating conditions, and a mathematical model based on the DPM-VOF coupled method was developed to predict the investigated multiphase phenomenon.

The DPM-VOF coupled method is also used to calculate the argon/steel/slag three-phase flow in the continuous casting mold, such as in Lopez et al.[27] and in Liu et al.[28] The Lagrangian DPM approach gives direct physical interpretation of the fluid-bubble interaction. However, it is computationally extensive hence cannot be used for simulating systems with high volume fraction of the dispersed phase. Some previous results have shown that the bubbles inside the mold are not clearly separated, but move as a conglomerate. However, it is difficult for the DPM model to characterize these high gas rate regions inside the mold. Although a lot of previous work[29–34] has been done on the subject of multiphase flow in the continuous casting mold, relatively little work[29] was reported on the slag eye formation in continuous casting mold.

In the present work, an Euler–Euler approach is developed to calculate the argon/steel/slag three-phase flow in the continuous casting mold. The calculation of the exposed slag eye is compared with the water model experiment and checked with the industrial observations.

2. Numerical Modeling

2.1. Model Assumption

1) The temperature field and the concentration field are not considered. The density and viscosity of all the phases are assumed to keep constant.
2) The slag layer in the continuous casting mold is divided into three layers; from top to bottom are the powder slag layer, the sintering layer, and the liquid slag layer. Only the liquid slag layer with better liquidity is considered.
3) Argon gas is injected into the SEN at a room temperature in actual production. It expands descending in the SEN due to heat transfer. Thus, the argon gas injection rate used in the model is the hot argon flow rate.[10] Because the size of argon bubbles is unknown, an uniform one of 1 mm is specified for all the bubbles entering the SEN. The breakup and coalescence of the bubbles are neglected.
4) All the phases are treated based on Eulerian approach: the molten steel and the liquid slag are considered as a continuous phase; the argon gas is assumed to be a dispersed one. **Figure 2** shows the interaction between phases for the Euler–Euler three-phase model. The drag force $\mathbf{F}_{ls}^{D}$ and surface tension force $\mathbf{F}_{ls}^{ST}$ are considered between steel and slag. The interfacial forces between dispersed argon bubble and continuous fluid (steel and slag) contains the drag $\mathbf{F}^{D}$, lift $\mathbf{F}^{L}$, virtual mass $\mathbf{F}^{VM}$, and turbulence dispersion force $\mathbf{F}^{TD}$.

2.2. Euler–Euler Argon/Steel/Slag Model

Three sets of conservation equations governing the mass and momentum are as follows:

$$\frac{\partial(\alpha_m\rho_m)}{\partial t} + \nabla\cdot(\alpha_m\rho_m\mathbf{u}_m) = 0 \qquad (1)$$

$$\frac{\partial(\alpha_m\rho_m\mathbf{u}_m)}{\partial t} + \nabla\cdot(\alpha_m\rho_m\mathbf{u}_m\mathbf{u}_m) = -\nabla\cdot(\alpha_m\tau_m) - \alpha_m\nabla P + \alpha_m\rho_m\mathbf{g} + \mathbf{F}_{nm} \qquad (2)$$

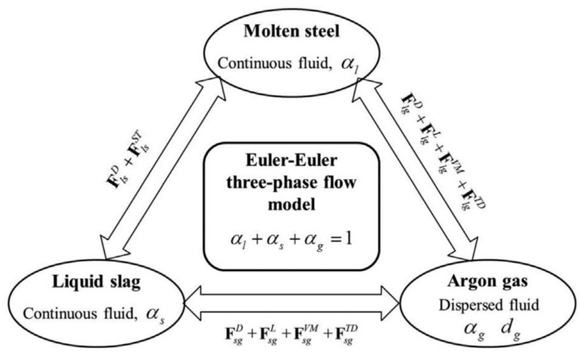

Figure 2. Interaction between phases for the current model.

where m and n are the phase index ($m = 1$: molten steel, $m = s$: liquid slag, $m = g$: argon gas), and $\alpha_l + \alpha_s + \alpha_g = 1$. ρ_m, $\mathbf{u}_m$ are density and velocity of each phase. All phases share a same pressure P. $\mathbf{F}_{nm}$ is the interfacial forces between two phases.

The deviatoric part of the stress tensor of the k phase is described as follows:

$$\tau_m = -\mu_{eff,m}\left(\nabla\mathbf{u}_m + (\nabla\mathbf{u}_m)^T - \frac{2}{3}\mathrm{I}(\nabla\cdot\mathbf{u}_m)\right) \tag{3}$$

where $\mu_{eff,m}$ is the effective viscosity. The effective viscosity of liquid phase is composed of the molecular viscosity $\mu_{M,m'}$, the turbulent viscosity $\mu_{T,m'}$, and an extra term due to bubble induced turbulence $\mu_{BI,m'}$.

$$\mu_{eff,m'} = \mu_{M,m'} + \mu_{T,m'} + \mu_{BI,m'} \tag{4}$$

where m' is the liquid phases ($m' = l$: molten steel, $m' = s$: liquid slag).

The gas effective viscosity is calculated based on the effective liquid viscosity,

$$\mu_{eff,g} = \alpha_l\frac{\rho_g}{\rho_l}\mu_{eff,l} + \alpha_s\frac{\rho_g}{\rho_s}\mu_{eff,s} \tag{5}$$

The homogeneous k–ε model is used to calculate the turbulent viscosity. In this case, a single turbulence field is solved for using a single turbulence model. The model proposed by Sato et al.[35] has been used to take into account of the turbulence induced by the movement of bubbles.

$$\mu_{t,m'} = C_\mu\rho_{m'}\frac{k^2}{\varepsilon} \tag{6}$$

$$\mu_{BI,m'} = C_{\mu,BI}\rho_{m'}\alpha_g d_g\left|\mathbf{u}_g - \mathbf{u}_l\right| \tag{7}$$

where the standard model constants $C_\mu = 0.09$, $C_{\mu,BI} = 0.6$. More details for the turbulent kinetic energy k and turbulent dissipation ε can be seen in previous works.[36,37]

2.3. Interfacial Forces

The interfacial forces exhibit an important effect in the Eulerian multiphase momentum equations. For the continuous fluids, molten steel (l) and liquid slag (s), the free surface model attempts to resolve the interface between the fluids. Thus only the drag force and surface tension force are considered between them. So the momentum exchange term $\mathbf{F}_{nm}$ in Equation 2 can be described as:

$$\mathbf{F}_{ls} = -\mathbf{F}_{sl} = \mathbf{F}_{ls}^D + \mathbf{F}_{ls}^{ST} \tag{8}$$

$$\mathbf{F}_{ls}^D = C_D\rho_{ls}A_{ls}|\mathbf{u}_s - \mathbf{u}_l|(\mathbf{u}_s - \mathbf{u}_l) \tag{9}$$

where $\mathbf{F}_{ls}^D$ is drag force, $\mathbf{F}_{ls}^{ST}$ is surface tension force. The mixture density is given by $\rho_{ls} = \alpha_l\rho_l + \alpha_s\rho_s$. C_D is the drag force coefficient. The drag force coefficient model of Zhang and Vanderheyden[38] was found to give better agreement with experimental data in previous work[9] of two-phase flow. So it is used in the current model.

$$C_D = 0.44 + \frac{24}{Re_g} + \frac{6}{1 + \sqrt{Re_g}} \tag{10}$$

A_{ls} is the interfacial area concentration. For the current three-phase flow, it is generalized as follows:

$$A_{ls} = \frac{2|\nabla\alpha_l|\cdot|\nabla\alpha_s|}{|\nabla\alpha_l| + |\nabla\alpha_s|} \tag{11}$$

The interfacial forces between dispersed argon bubble and continuous fluid (molten steel and liquid slag) contains the drag, lift, virtual mass, and turbulence dispersion force. The momentum exchange term is given as follows:

$$\mathbf{F}_{m'g} = -\mathbf{F}_{gm'} = \mathbf{F}_{m'g}^D + \mathbf{F}_{m'g}^L + \mathbf{F}_{m'g}^{VM} + \mathbf{F}_{m'g}^{TD} \tag{12}$$

A brief description of each interfacial force component is presented below.

$$\mathbf{F}_{m'g}^D = -\frac{3}{4}\alpha_g\rho_{m'}\frac{C_D}{d_g}\left|\mathbf{u}_g - \mathbf{u}_{m'}\right|(\mathbf{u}_g - \mathbf{u}_{m'}) \tag{13a}$$

$$\mathbf{F}_{m'g}^L = \alpha_g\rho_{m'}C_L\left(\mathbf{u}_g - \mathbf{u}_{m'}\right)\times\nabla\times\mathbf{u}_{m'} \tag{13b}$$

$$\mathbf{F}_{m'g}^{VM} = \alpha_g\rho_{m'}C_{VM}\left(\frac{D\mathbf{u}_g}{Dt} - \frac{D\mathbf{u}_{m'}}{Dt}\right) \tag{13c}$$

$$\mathbf{F}_{m'g}^{TD} = C_{TD}C_D\frac{\mu_{t,g}}{\sigma_{t,g}}\left(\frac{\nabla\alpha_{m'}}{\alpha_{m'}} - \frac{\nabla\alpha_g}{\alpha_g}\right) \tag{13d}$$

where C_L is the lift force coefficient. It is set to 0.5 based on the work of Drew and Lahey.[39] C_{VM} is the virtual mass force coefficient, which is taken to be 0.5 for individual spherical bubbles.[40] By default,[41] the turbulent dispersion coefficient $C_{TD} = 1$ and the turbulent Schmidt number $\sigma_{t,g} = 0.9$ are adopted.

2.4. Continuum Surface Force (*l*–*s*)

Surface tension is a key force for the level fluctuation and the formation of exposed slag eye. When the interface energy is not constant, the surface tension force has a tangential component that tends to move fluid along the interface toward regions of high surface tension. In this model, the continuum surface force model proposed by Brackbill et al.[42] was used to consider the effect of surface tension at the interface between steel and slag. The surface tension is modeled as a volume force concentrated at the interface, rather than a surface force, which is defined as:

$$\mathbf{F}_{ls}^{ST} = -\sigma_{ls}\kappa_{ls}\mathbf{n}_{ls}\delta_{ls} \tag{14}$$

where σ_{ls} is the surface tension coefficient; κ_{ls} is the surface curvature defined by $\kappa_{ls} = \nabla \cdot \mathbf{n}_{ls}$; $\mathbf{n}_{ls}$ is the interface normal vector pointing from the primary fluid (steel) to the secondary fluid (slag) which is calculated from the gradient of a smoothed volume fraction; δ_{ls} is the interface delta function; it is zero away from the interface, thereby ensuring that the surface tension force is active only near to the interface.

2.5. Boundary Conditions

The computational cost is reduced due to the symmetry of the geometry by modeling only a quarter of the domain; the numerical grid of about 600 000 cells, as shown in **Figure 3**, is used. The initial slag layer thickness is 25 mm. The free space above the slag layer is filled with the argon gas, and the initial thickness is 50 mm. The fluid properties and operating conditions used in water model and numerical simulation are listed in **Table 1**. A mass flow boundary condition for the molten

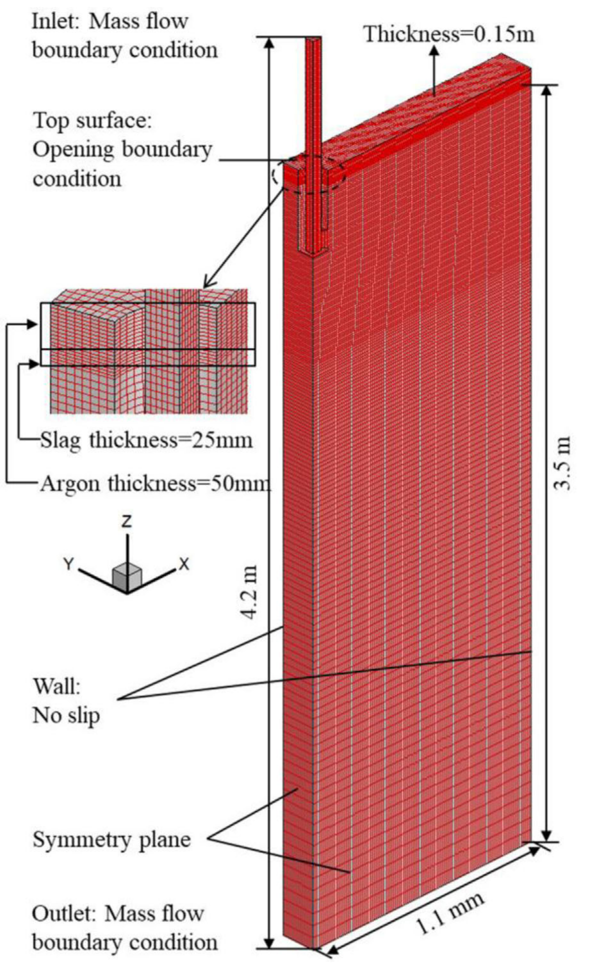

Figure 3. Schematics of the simulation domain and boundary conditions.

Table 1. Geometrical, physical properties, and operating conditions in water model and steel caster.

Parameter	1/4th Water model	Steel caster
Mold width × thickness	$550 \times 75\ mm^2$	$2200 \times 300\ mm^2$
Mold/Strand height	900 mm	Open bottom
Diameter of SEN	20 mm	80 mm
Length of SEN	305 mm	1220 mm
Exit angle of nozzle	15° down	15° down
SEN port height × Width	$20 \times 17.5\ mm^2$	$80 \times 70\ mm^2$
Submergence depth of SEN	75 mm	300 mm
Liquid density	$1000\ kg\ m^{-3}$	$7020\ kg\ m^{-3}$
Liquid viscosity	$0.001\ kg\ m^{-1}\ s^{-1}$	$0.0056\ kg\ m^{-1}\ s^{-1}$
Slag density	$-900\ kg\ m^{-3}$	$2600\ kg\ m^{-3}$
Slag viscosity	$0.042\ kg\ m^{-1}\ s^{-1}$	$0.09\ kg\ m^{-1}\ s^{-1}$
Gas density	$1.2\ kg\ m^{-3}$	$0.56\ kg\ m^{-3}$
Gas viscosity	$1.82 \times 10^{-5}\ kg\ m^{-1}\ s^{-1}$	$7.42 \times 10^{-5}\ kg\ m^{-1}\ s^{-1}$

steel and argon gas is defined at the inlet of the SEN based on the casting speed and gas injection rate. A mass flow boundary condition is also applied at the bottom of the calculation domain. The top surface of the mold cavity is modeled as a degassing boundary condition, where the gas phase can escape, but there is no liquid flux. Along the walls, no-slip conditions with the standard wall function are adopted. A fixed time step of 0.005 s is adopted for all the transient calculations. In order to keep the interface sharp, a compressive differencing scheme is used for the advection term in the continuity equations. An implicit time-stepping scheme of the second order backward Euler scheme is used in this model.

3. Physical Modeling

Since the kinematic viscosity of water at 298 K is almost equal to molten steel at 1873 K, water is widely used to replicate the fluid flow observed for the molten steel. In the current work, a one-fourth scaled water model is established to physically simulate the bubble distribution and the formation of exposed slag eye in a thick slab continuous casting mold. Table 1 gives operational details on the water model and the corresponding actual steel caster performance.

Water and nitrogen (N_2) are respectively used to simulate molten steel and argon gas, while the liquid slag is simulated by bean oil. Water flow rate used in the experiment corresponding to actual throughput in the caster was obtained based on the normal Froude similarity number:

$$Fr = \frac{u_l^2}{gL} \tag{15}$$

$$Q_{water,298K} = 0.03125 Q_{steel,1873K} \tag{16}$$

Volume expansion due to the heating of injected argon gas (298 K) to molten steel temperature (1873 K) has been considered. The modified Froude similarity number was used to obtain the N_2 flow rate:

$$Fr_m = \frac{u_l^2}{gL}\frac{\rho_g}{\rho_l - \rho_g} \tag{17}$$

$$Q_{Argon,1873K} = \frac{1873K}{298K} Q_{Argon,298K} = 6.285 Q_{Argon,298K} \tag{18}$$

$$Q_{N_2,298K} = 0.052 Q_{Argon,298K} \tag{19}$$

The top slag layer in the water model is chosen based on the following dimensionless analysis:

$$\frac{v_{slag}}{v_{steel}} = \frac{v_{oil}}{v_{water}} \tag{20}$$

The viscosity ratio for the bean oil-water system was found to be close to that of slag-steel system.

When the three-phase flow inside the mold reached its quasi-steady state, the formed exposed slag eyes were recorded using a video recorder and the distributions of gas bubbles were captured by a high-speed camera with 1000 fps using a laser light-sheet, which was positioned at the axial-symmetrical plane of the mold, parallel to the wide face.

4. Results and Discussion

4.1. Gas Volume Fraction Characteristics

Figure 4 shows the simulation results for the instantaneous argon volume fraction distribution at the central cross-section of the mold. The casting speed is 0.6 m min^{-1}, argon injection rate is 4 l min^{-1} under normal conditions, and the thickness of the initial slag layer on the top of molten steel pool is 25 mm. Due to the limitation of post-processing method, the slag layer is not shown in this figure; an additional picture for $\alpha_s = 0.5$ iso-surface of slag phase was added on the right side of the figure to show the distribution of slag layer. Compared with the gas bubble distribution in the water model obtained by a high-speed camera, it can be seen from the whole figure that the phenomenon of high gas volume fraction ($\alpha_g \geq 0.5$) at the upper part of SEN port is captured well by the numerical model. After the argon gas flows out of the SEN port, it partially floats directly upwards till the top surface along the SEN and escapes through the slag layer. The argon gas, traveling with the melt flow beneath the meniscus, gradually accumulates and breaks through the slag layer if a form of a plume at specific critical spot, inducing significant level fluctuation and in a critical case even forming the exposed slag eye.

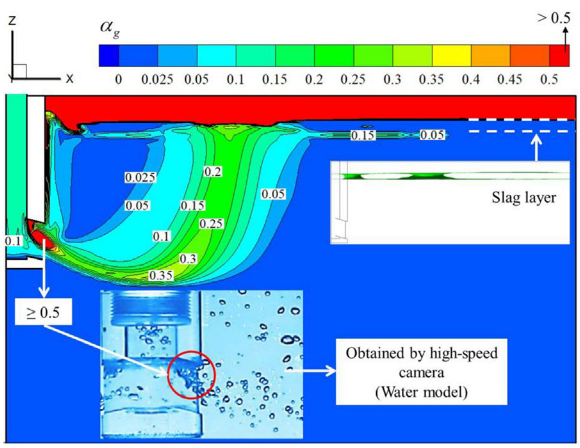

Figure 4. Instantaneous argon volume fraction in the mold.

Figure 5 shows the argon volume fraction distribution at different cross sections of the slag layer. At the top surface of the slag layer, in Figure 5a, two concentrated escape areas for the argon gas ($\alpha_g > 0.3$) were found near the SEN and at 0.4 m away from the SEN. Several small open spots ($\alpha_g < 0.005$) were found around 0.8 m away from the SEN, which follow the water model observations, as shown in **Figure 6**a. Figure 5b shows the argon volume fraction distribution at the middle-section of the slag layer. Compared with Figure 5a, a decreased gas concentration is detected ($\alpha_g > 0.3$), and the area of possible eye formation increases. At the bottom of the slag layer, presented in Figure 5c, the gas distribution is even more diffused, and no defined location of a plume formation can be specified. In other words, many argon bubbles stay under the slag layer and travel along the interface, which is similarly reported by the results of water modeling, as shown in Figure 6b. Additionally, according to the experiment a lot of bubbles reside at the liquid/slag interface, especially at the areas of the emulsified slag. This phenomenon occurring during gas injection is not considered in the present model.

A sketch on the right side of Figure 5 shows the bubble floatation inside the slag layer, indicating that argon gas would gradually gathered together up to the top of the plume: the bubble number inside each control volume significantly grows starting with much dispersed distribution at the steel/slag interface and becomes very dense at the eye opening. The phase interaction mechanism, namely the slag resistance, is the essence of such a phenomenon. Moreover, if the gas concentration area is distributed, that causes a formation of several exposed eyes, as can be observed at the experimental picture in Figure 6a.

4.2. Formation of the Exposed Slag Eye

Multiphase flow simulation results, showing the prediction of the exposed slag eye phenomenon in the continuous casting mold, are presented in **Figure 7**. A velocity vector field of the molten steel is given for the central cross-section; it can be observed that the melt partially moves toward the top surface immediately after leaving the SEN port; that motion is enhanced by the floatation of the argon gas due to the strong drag force. The rest of the melt forms a jet impinging the mold's narrow wall. An iso-surface of $\alpha_s = 0.5$ is used to indicate two exposed slag eyes: one is adjacent to the SEN and another is located approximately halfway toward the narrow wall, corresponding to the position of most argon escaping in Figure 5a. It can be found

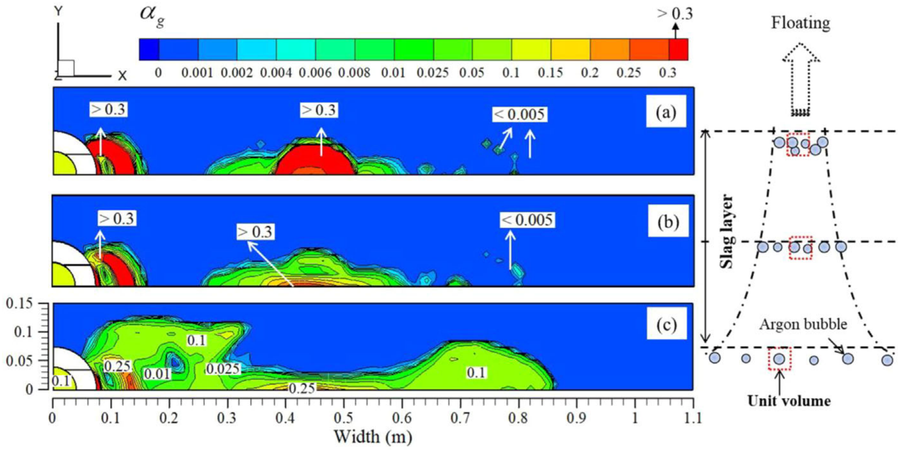

Figure 5. Argon volume fraction distribution at different cross-sections of the slag layer: a) top, b) middle, and c) bottom section.

that the position and the size of the openings agree well with those taken from the industrial observation (Figure 1).

The covering of the top surface by the slag layer as well as the argon distribution in the central cross-section are shown in **Figure 8**. The results of the simulation correspond to two different gas injection rates of 21 and 43 l min^{-1}, respectively. For both cases the casting speed of 0.6 m min^{-1} and the initial slag thickness of 25 mm are taken; the uniform bubble diameter of 1 mm is assumed; injection rate are estimated for the hot gas. At low gas injection rate (21 l min^{-1}), see Figure 8a, the slag layer covers most of the top surface; only a small exposed area is formed adjacent to the SEN. In the upper flow region close to the slag, the injected gas tends to float up at about 0.45 m in direction toward the narrow wall; however its momentum is too low to break through the slag layer and no opening is detected in that case. With growing gas flow rate (up to 43 l min^{-1}), as shown in Figure 8b, a bigger opening develops near the SEN, as well as the second slag eye finally forms at the location mentioned previously. Additionally, the modeling results show that both openings expand with increasing argon injection rate; however the opening adjacent to the SEN is not so strongly influenced, as the second opened eye.

Figure 9 shows the argon volume fraction distribution at the centreline of the initial horizontal steel/slag interface along the mold's width corresponding to different argon injection rates. For all the cases, the argon volume fraction is very high near the SEN, which explains the formation of exposed slag eye here even at the lowest inlet argon flux. Another peak concentration of the gas is located at about 0.45 m from the SEN, fitting to the location of the second slag eye. It can be seen that the argon volume fraction grows from 13% to 30% when the injection rate increases from 21 to 98 l min^{-1}.

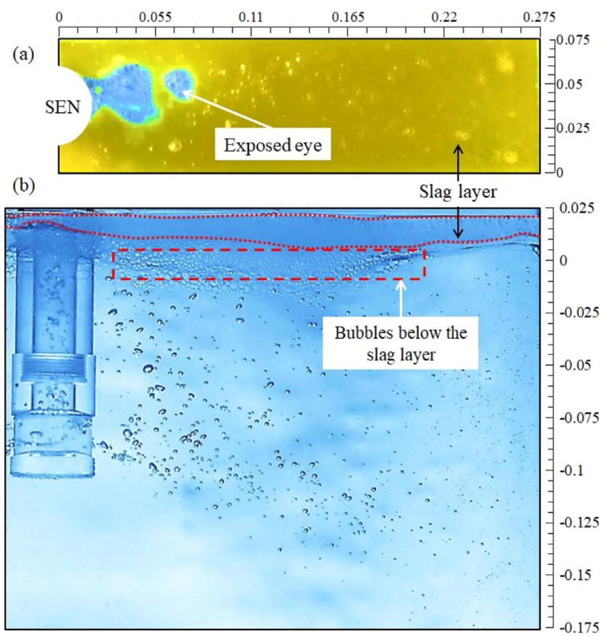

Figure 6. Water model observation of the exposed slag eye a) and bubble distribution b).

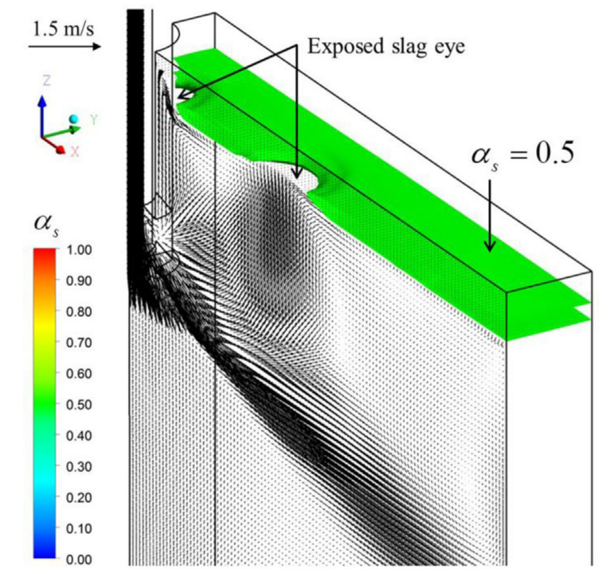

Figure 7. Transient flow field and exposed slag eye phenomenon.

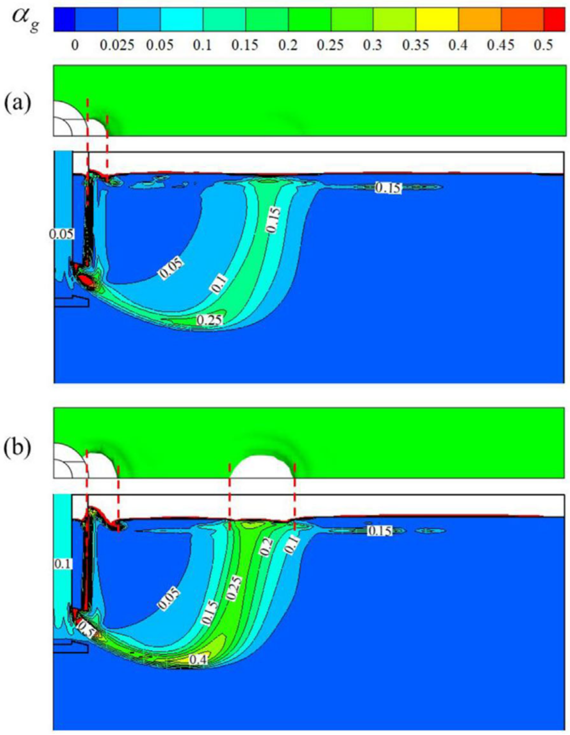

Figure 8. Slag layer coverage and argon volume fraction at different argon flow rates: a) 21 l min^{-1} and b) 43 l min^{-1}.

The turbulent kinetic energy of the molten steel phase at the centreline of the initial horizontal steel/slag interface is shown in **Figure 10**. For the different argon injection rates only two main peak values are detected: adjacent to the SEN and at the position of the second slag eye development. They become more defined with the growing gas rate. It indicates that the effect of argon gas on the steel jet is noteworthy and should not be ignored in the mathematical model. It should also be mentioned, that five kinds of interfacial forces are already considered in the current Eulerian model, whereas more detailed investigation is still required. For low gas injection rate (21 l min^{-1}), the maximum

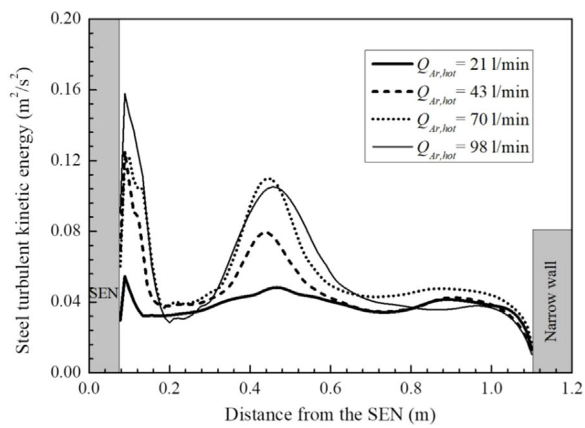

Figure 10. Turbulent kinetic energy of steel along the centreline of the initial horizontal steel/slag interface.

value of the turbulent kinetic energy of the molten steel close to the SEN reaches 0.0545 m^2 s^{-2} and the exposed slag eye is formed. The peak value at 0.483 m from the SEN is 0.0483 m^2 s^{-2}, and no slag opening is observed. When the gas injection rate increases to 43 l min^{-1}, the melt flow kinetic energy increases dramatically at the locations of the exposed eyes, which can be seen in Figure 8b. It indicates that the melt is able to break through the slag layer.

Time-averaged level fluctuations of the steel/slag interface are given in **Figure 11**. For the considered simulation cases, the convex meniscus is observed both close to the SEN and 0.45 m away from the nozzle (second eye location), but it becomes concave near the narrow wall. The increase of the argon injection rate promotes a gradual melt elevation at the middle of the mold at the slag opening. For the highest gas rate of 98 l min^{-1} the interface rises directly from the SEN till the position 0.65 m along the mold width. Further a monotonically descends of the interface is observed till the melt reaches the narrow wall. Such a strong deformation of the meniscus is due to the high amount of the argon gas simultaneously occupying significant volume of the liquid pool underneath the slag band. For the lowest gas injection rate (21 l min^{-1}), the fluctuation height at the critical

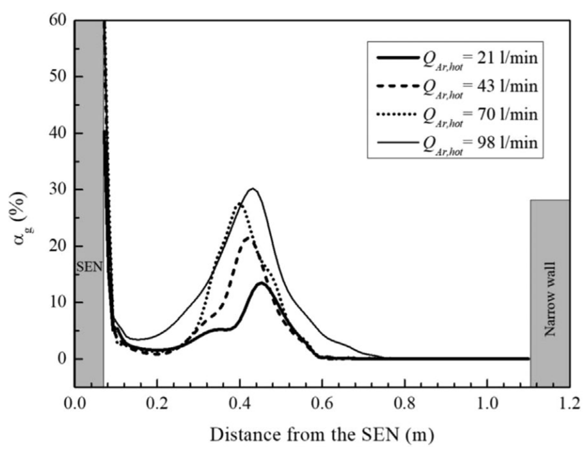

Figure 9. Argon volume fraction along the centreline of the initial horizontal steel/slag interface for various gas injection rates.

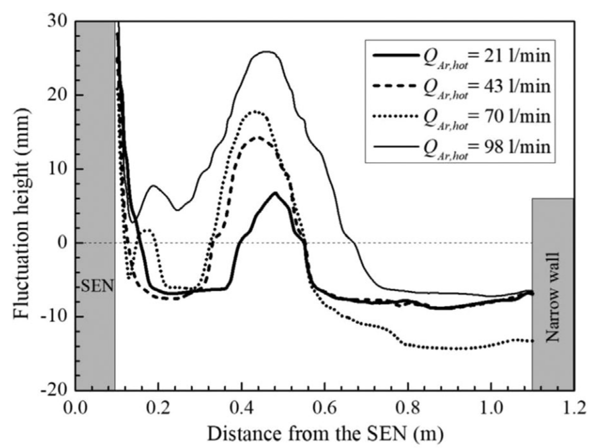

Figure 11. Time-averaged fluctuations along the centreline of steel/slag interface.

spot (0.483 m from the SEN) is about 6.8 mm, and no exposed slag eye is detected until argon injection reaches 43 l min^{-1} and the slag opening occur at 0.45 m from the SEN with the meniscus elevation of 13.9 mm.

The presented observations emphasize the importance of the key parameter for the exposed slag eye formation, namely – the argon gas injection rate. For the continuous casting conditions used in the current studies, a critical amount of fluctuation height between 6.8 and 13.9 mm can be defined as the limits for the formation of the slag eye. However, a critical amount of argon gas will vary from case to case and additional studies are required to establish the unified criterion for the slag eye formation in the continuous casting mold.

4.3. Effect of the Bubble Size

As it is discussed in the previous sections of this work, the argon gas injection practice during the continuous casting process strongly affects the molten steel flow pattern and promotes the meniscus level fluctuation to the critical limits when the exposed slag eye can appear. Further, the extent of considered influence depends both on the gas injection rate and on the bubble size distribution. Moreover, the last one is mostly independent of the gas injection rate and continuously changes due to the coalescence and break up mechanisms been involved. The predicted slag layer coverage of the mold's top surface is presented in **Figure 12** for the different simulated argon bubble sizes. For all the cases, the casting speed of 0.6 m min^{-1}, gas injection rates of 43 l min^{-1}, and initial slag thickness of 25 mm are taken.

For the case of the smallest bubbles been modeled ($d_g = 0.5$ mm) two slag openings are found, please refer to Figure 12a. With growing bubble diameter the exposed eye in the mid-section of the mold sequentially decreases in size and shifts toward the SEN; the slag opening near the SEN remains mostly unchanged. The argon volume fraction along the centreline of the initial horizontal steel/slag interface for various bubble sizes is shown in **Figure 13**. One can see, that the smaller bubbles are, further they can travel towards the narrow wall with the melt jet beneath the slag layer before their floatation completes; the dispersion of the smaller bubbles is wider as well. For the biggest diameter $d_g = 3$ mm (see Figure 12d) the formation of the second

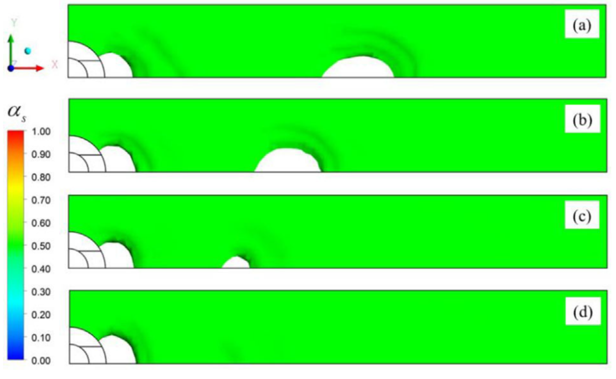

Figure 12. Slag layer covering top surface based. Results for different bubble sizes: a) 0.5 mm, b) 1 mm, c) 2 mm, and d) 3 mm.

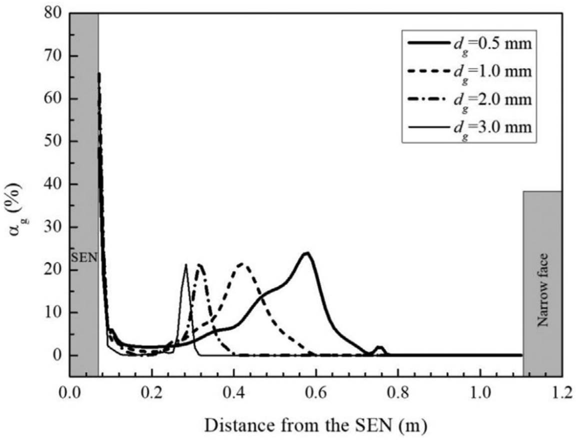

Figure 13. Argon volume fraction along the centreline of the initial horizontal steel/slag interface for various bubble sizes.

exposed eye is even suppressed; however the slag coverage is disturbed for all the cases at the proximity of the SEN due to the high argon volume. It immediately escapes from the port outlet along the refractory walls forming a dense gas plume, which pushes the slag layer away.

The effect of the argon bubble size on the level fluctuation of steel/slag interface are gathered in **Figure 14**. Due to the large gas concentration near the SEN, the level fluctuations close to the SEN are always high. With the biggest bubble diameter $d_g = 3$ mm the highest elevation value of 4.6 mm is located at 0.33 m from the SEN; however no exposed slag eye is formed. As the argon bubble size decreases down to 0.5 mm, the peak value of the level fluctuation increases up-to 17.6 mm and strongly exposed opening is developed. Thereby the argon bubble size is very important for the accurate prediction of the multiphase flow; however the bubble size distribution[43,44] inside the mold requires further investigation.

Based on the results presented in Figure 11, an approximate criterion of argon gas injection rate (between 21 and 43 l min^{-1}) can be established to estimate the conditions at which the exposed slag eye is formed. However, more detailed and general

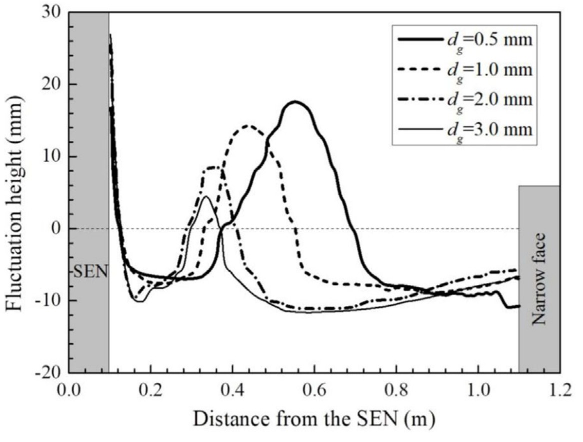

Figure 14. Time-averaged interface fluctuation height for different argon bubble sizes.

criterion requires further research considering additional factors, such as casting speed, submerged depth, port angle of the SEN, thickness of the slag layer, etc.

5. Conclusions

In the presented study an Euler–Euler model is developed to predict the argon/steel/slag three-phase flow and the formation of the exposed slag eye in a slab continuous casting mold. The conclusions obtained are summarized as follows:

1) Two characteristic patterns of the argon gas motion in the melt pool are defined: i) immediate floatation along the SEN wall towards a free surface; ii) transversal motion of the bubbles toward the narrow wall driven by the melt jet and submeniscus flow including their further escape through the slag layer.
2) Two kinds of exposed slag eyes are observed during the plant trials: a smaller one is adjacent to the SEN and the bigger one located at about 0.4 m away from the nozzle. Similar phenomena are caught both in the water model experiments and predicted by the applied numerical model.
3) The gas injection rate is a key parameter for the formation of exposed slag eye. For the continuous casting conditions used in the current study, an approximate criterion of argon gas injection rate (between 21 and 43 $\mathrm{l\,min^{-1}}$) was found to be a characteristic value below which the formation of the mid-section slag opening is suppressed.
4) Bubble size is another key parameter for the accurate predication of the multiphase flow during the steel casting process. Investigations show, that as the argon bubble size drops, the size of the mid-section exposed slag eye increases, and its location shifts closer to the mold's narrow wall. The near-SEN eye shape is barely influenced by the bubble size as well as the injection rate has slight effect on it.
5) Some mismatches with the experimental and industrial observation could be due to more complex real bubble size distribution, affected by their coalescence and breakup, which are not considered in the current model and require further investigations.
6) The near-SEN exposed eye occurs under any of considered conditions. The one at the mid-section is formed when the meniscus convex reaches a critical level, been dependent on the casting conditions.

Acknowledgments

This work was financially supported by the National Natural Science Foundation of China (No. 51604070 and No. 51574068), Funding from the China Scholarship Council for study abroad (No. 201706085027). The financial support by RHI-M AG, the Austrian Federal Ministry of Economy, Family and Youth, and the National Foundation for Research, Technology and Development is gratefully acknowledged.

Conflict of Interest

The authors declare no conflict of interest.

Nomenclatures

C_μ, $C_{\mu,BI}$	Model constant, dimensionless
C_D	Drag coefficient, dimensionless
C_L	Lift coefficient, dimensionless
C_{VM}	Virtual mass coefficient, dimensionless
C_{TD}	Turbulent dispersion coefficient, dimensionless
d_g	Bubble diameter, [m]
$\mathbf{F}_k$	Momentum exchange term, [N m^{-3}]
$\mathbf{F}^D$	Drag force, [N m^{-3}]
$\mathbf{F}^L$	Lift force, [N m^{-3}]
$\mathbf{F}^{ST}$	Surface Tension force, [N m^{-3}]
$\mathbf{F}^{TD}$	Turbulent dispersion force, [N m^{-3}]
$\mathbf{F}^{VM}$	Virtual mass force, [N m^{-3}]
$\mathbf{g}$	Acceleration of gravity, [m s^{-2}]
I	Unity tensor
k	Turbulent kinetic energy, [m^2 s^{-2}]
L	Characteristic length, [m]
P	Static pressure, [Pa]
Q	Volume flow rate, [m^3 s^{-1}]
t	Time, [s]
$\mathbf{u}$	Velocity of fluid phase, [m s^{-1}]
ρ	Density of fluid, [kg m^{-3}]
μ_{eff}	Effective viscosity, [N s m^{-2}]
μ_M	Molecular viscosity of liquid phase, [N s m^{-2}]
μ_T	Turbulent viscosity, [N s m^{-2}]
μ_{BI}	Bubble induced viscosity, [N s m^{-2}]
α	Volume fraction, dimensionless
σ_t	Turbulent Schmidt number, dimensionless
ν	Kinematic viscosity, [m^2 s^{-1}]
ν_t	Turbulence kinematic viscosity, [m^2 s^{-1}]
$\boldsymbol{\tau}$	Shear stress
ε	Turbulent dissipation rate, [m^2 s^{-3}]

Subscripts

g	Gas phase
l	Liquid slag phase
s	Molten steel phase
m,m'	Gas, molten steel, or liquid slag phase

Keywords

continuous casting mold, Euler–Euler approach, exposed slag eye, three-phase flow

Received: February 25, 2018
Published online: May 30, 2018

[1] B. G. Thomas, *Steel Res. Int.* **2018**, *89*, srin. 1700312. https://doi.org/10.1002/srin.201700312
[2] M. Iguchi, N. Kashi, *Metall. Mater. Trans. B* **2000**, *31*, 453.
[3] B. G. Thomas, L. F. Zhang, *ISIJ Int.* **2001**, *41*, 1181.
[4] K. C. Mills, A. B. Fox, *ISIJ Int.* **2003**, *43*, 1479.

[5] A. Harloff, O. Pütz, S. Rödl, R. Striedinger, D. Sucker, *Steel Res. Int*. **2005**, *76*, 13.
[6] P. D. Lee, P. E. Ramirez-Lopez, K. C. Mills, B. Santillana, *Ironmaking Steelmaking* **2012**, *39*, 244.
[7] Z. Q. Liu, B. K. Li, *Powder Tech*. **2018**, *323*, 403.
[8] A. Ramos-Banderas, R. D. Morales, R. Sanchez-Perez, L. Garcia-Demedices, G. Solorio-Diaz, *Int. J. Multiphase Flow* **2005**, *31*, 643.
[9] Z. Q. Liu, B. K. Li, *Metall. Mater. Trans. B* **2017**, *48*, 1833.
[10] Z. Q. Liu, B. K. Li, M. F. Jiang, F. Tsukihashi, *ISIJ Int*. **2013**, *53*, 484.
[11] K. Yonezawa, K. Schwerdtfeger, *Metall. Mater. Trans. B* **1999**, *30*, 411.
[12] K. Yonezawa, K. Schwerdtfeger, *Metall. Mater. Trans. B* **2000**, *31*, 461.
[13] Subagyo, G. A. Brooks, G. A. Irons, *ISIJ Int*. **2003**, *43*, 262.
[14] M. Iguchi, K. I. Miyamoto, S. Yamashita, D. Iguchi, M. Zeze, *ISIJ Int*. **2004**, *44*, 636.
[15] D. Mazumdar, J. W. Evans, *Metall. Mater. Trans. B* **2004**, *35*, 400.
[16] K. Krishnapisharody, G. A. Irons, *Metall. Mater. Trans. B* **2006**, *37*, 763.
[17] K. Krishnapisharody, G. A. Irons, *Metall. Mater. Trans. B* **2015**, *46*, 191.
[18] Z. Q. Liu, L. M. Li, B. K. Li, *ISIJ Int*. **2017**, *57*, 1971.
[19] B. Li, H. Yin, C. Zhou, F. Tsukihashi, *ISIJ Int*. **2008**, *48*, 1704.
[20] C. A. Llanos, S. Garcia, J. A. Ramos-Banderas, J. D. J. Barreto, G. Solorio, *ISIJ Int*. **2010**, *50*, 396.
[21] S. W. P. Cloete, J. J. Eksteen, S. M. Bradshaw, *Miner. Eng*. **2013**, *46*, 16.
[22] H. Liu, Z. Qi, M. Xu, *Steel Res. Int*. **2011**, *82*, 440.
[23] L. M. Li, B. K. Li, Z. Q. Liu, *ISIJ Int*. **2017**, *57*, 1980.
[24] K. Chattopadhyay, M. Hasan, M. Isac, R. I. L. Guthrie, *Metall. Mater. Trans. B* **2010**, *41*, 225.
[25] S. Chatterjee, K. Chattopadhyay, *Metall. Mater. Trans. B* **2016**, *47*, 3099.
[26] S. Chatterjee, D. Li, K. Chattopadhyay, *Steel Res. Int*. **2017**, *88*, No. 9.
[27] P. E. R. Lopez, P. N. Jalali, J. Bjorkvall, U. Sjostrom, C. Nilsson, *ISIJ Int*. **2014**, *54*, 342.
[28] Z. Q. Liu, Z. B. Sun, B. K. Li, *Metall. Mater. Trans. B*. **2017**, *48*, 1248.
[29] H. Bai, B. G. Thomas, *Metall. Mater. Trans. B* **2001**, *32*, 1143.
[30] R. Sánchez-Perez, R. D. Morales, M. Diaz-cruz, O. Olivares-xometl, J. Palafox-ramos, *ISIJ Int*. **2003**, *43*, 637.
[31] M. Saeedipour, S. Puttinger, N. Doppelhammer, S. Pirker, *Proceedings of the 8th European Continuous Casting Conference*, Graz, Austria **2014**.
[32] A. Vakhrushev, M. H. Wu, A. Ludwig, G. Nitzl, Y. Tang, G. Hackl, *Proceedings of the 8th European Continuous Casting Conference*, Graz, Austria, **2014**.
[33] K. Timmel, N. Shevchenko, M. Roder, M. Anderhuber, P. Gardin, S. Eckert, G. Gerbeth, *Metall. Mater. Trans. B* **2015**, *46*, 700.
[34] Z. Q. Liu, B. K. Li, M. F. Jiang, F. Tsukihashi, *ISIJ Int*. **2014**, *54*, 1314.
[35] Y. Sato, M. Sadatomi, K. Sekiguchi, *Int. J. Multiphase Flow* **1975**, *2*, 79.
[36] Z. Q. Liu, F. S. Qi, B. K. Li, M. F. Jiang, *J. Iron Steel Res. Int*. **2014**, *21*, 1081.
[37] Z. Q. Liu, B. K. Li, *J. Chem. Eng. J*. **2018**, *338*, 465.
[38] D. Z. Zhang, W. B. Vanderheyden, *Int. J. Multiphase Flow* **2002**, *28*, 805.
[39] D. A. Drew, R. T. Lahey, *Int. J. Multiphase Flow* **1987**, *13*, 113.
[40] D. A. Drew, L. Cheng, R. T. Lahey, *Int. J. Multiphase Flow* **1979**, *5*, 233.
[41] A. D. Burns, T. Frank, I. Hamill, J. Shi, *Proceeding of the Fifth International Conference on Multiphase Flow*, Yokohama, Japan **2004**.
[42] J. U. Brackbill, D. B. Kothe, C. Zemach, *J. Comput. Phys*. **1992**, *100*, 335.
[43] Z. Q. Liu, L. M. Li, F. S. Qi, B. K. Li, M. F. Jiang, F. Tsukihashi, *Metall. Mater. Trans. B* **2015**, *46*, 406.
[44] Z. Q. Liu, B. K. Li, F. S. Qi, S. C. P. Cheung, *Powder Tech*. **2017**, *319*, 139.

